Interactive 3-D visual analysis of ERA 5 data: improving diagnostic indices for marine cold air outbreaks

Marcel Meyer[1,3], Iuliia Polkova[2,3], Kameswar Rao Modali[1], Laura Schaffer[2], Johanna Baehr[2,3], Stephan Olbrich[1,3], and Marc Rautenhaus[1,3]

[1]Regional Computing Centre, Visual Data Analysis Group, Universität Hamburg, Germany
[2]Institute of Oceanography, Universität Hamburg, Germany
[3]Center for Earth System Research and Sustainability (CEN), Universität Hamburg, Germany

Correspondence: Marcel Meyer (marcel.meyer@uni-hamburg.de)

Abstract. We inspect the 3-D structure of Marine Cold Air Outbreaks (MCAOs) and Polar Lows (PLs) in ERA5 data with the aim of improving diagnostic indices to capture these weather events in long-term assessments on seasonal and climatological time-scales. For this study, we designed a workflow that starts with the interactive 3-D visual exploration of single MCAO and PL events, using an extended version of the open-source visualization framework *Met.3D*, followed by the design and statistical testing of new diagnostic indices in long-term assessments. Results from the interactive visual data exploration provide insights into the complex 3-D shape and dynamics of MCAOs and PLs in ERA5 data. Motivated by the visual analysis of single cases, we extend widely-used diagnostics by conceptualizing a simple index to capture the vertical extent of the lower-level instability induced by MCAOs. Testing the association of diagnostic indices with observed PLs in the Barents and the Nordic Seas (STARS data) shows that, the new MCAO index introduced here has an important advantage: it is a more skillful indicator for distinguishing the times and locations of PLs, compared with previously-used indices. We thus propose the new index for further analyses in seasonal climate predictions and climatological studies. The methods for interactive 3-D visual data analysis presented here are available as a generic open-source tool for investigating atmospheric processes in ERA5 and other gridded meteorological data.

1 Introduction

Marine Cold Air Outbreaks (MCAOs) are transport events of cold air from sea-ice or snow-covered regions towards relatively warmer oceans (Rasmussen, 1983; Kolstad and Bracegirdle, 2008; Gryschka, 2018; Polkova et al., 2021). Understanding MCAOs is relevant because they represent conditions favourable for extreme weather phenomena known as Polar Lows (PLs) (Rasmussen, 1983; Ese et al., 1988; Kolstad, 2011; Michel et al., 2018). PLs are intense mesoscale cyclones, which have been called "Arctic hurricanes" (Nordeng, 1992; Føre et al., 2012; Bracegirdle, 2012), because some of them exhibit similarities to tropical hurricanes, such as symmetric vortex-like cloud patterns. PLs in the Northern Hemisphere usually occur during winter and are characterized by strong winds, heavy precipitation and severe marine icing, which pose substantial risks to marine activities and infrastructure (Aarnes et al., 2018). In addition to representing conducive conditions for extreme weather, MCAOs are also important in the context of deep water formation as they contribute to cooling of the ocean surface (Papritz and Spengler,

2017). In this study, we designed a workflow starting with interactive 3-D visual analysis of the ERA5 atmospheric reanalysis
25 data for improving our understanding of MCAOs and PLs and the diagnostics used to capture these events in long-term studies.

Recent advances in meteorological modelling, visualization techniques and computational performance provide new means
for the interactive exploration of 3-D features of weather phenomena in gridded meteorological data (Rautenhaus et al., 2018).
The global reanalysis dataset ERA5 (in what follows referred to as ERA5), which has recently been released by the Euro-
30 pean Centre for Medium-Range Weather Forecast (ECMWF), is considered to be the most detailed and highest quality global
climatological reanalysis data available (Hersbach et al., 2020; Copernicus Climate Change Service (C3S), 2017). The in-
creased spatial and temporal resolution of ERA5, compared with its predecessors, allows for resolving many 3-D features of
meteorological phenomena with a level of detail that was previously unattainable. Recent advances in techniques for visual
data exploration, leveraging the increased computational power of GPUs, enable the interactive visual analysis (IVA) of 3-D
35 atmospheric features in gridded meteorological data. Open-source visualization frameworks suited for meteorological applica-
tions include *ParaView* (Ayachit, 2015), *Vapor* (Clyne et al., 2007) and *Met.3D* (Rautenhaus et al., 2015b,a). In this study, we
apply *Met.3D*, which offers the key advantage of enabling quick interactive 3-D data exploration, powered by GPU implemen-
tations of core visualization algorithms. In contrast to standard 2-D visualisations, interactive 3-D data exploration provides
more realistic impressions, for example by sliding horizontal or vertical cross-sections through data volumes or by computing,
40 on-the-fly, various 3-D isosurfaces that can be adapted interactively. Interactive exploration of meteorological data can help
improving our understanding of meteorological phenomena as it allows analysing known data features in three dimensions,
quickly investigating system dependencies, and, importantly, exploring unknown features for formulating new hypotheses in
areas of active research.

45 Characterizing MCAOs by simple diagnostic indices and understanding the link between MCAOs and PLs is an area of active
research with relevance for improving seasonal predictions and climatological analyses. Various interdependent factors play a
role in the genesis of MCAOs and PLs (Claud et al., 2007; Kolstad and Bracegirdle, 2008; Kolstad, 2011; Terpstra et al., 2016;
Afargan-Gerstman et al., 2020; Stoll et al., 2021). MCAOs have been reported to be a necessary, but not a sufficient condition for
the occurrence of PLs (Kolstad, 2011). However, a recent climatological study has not found a robust link between conventional
50 cold air outbreak indices and the occurrence of polar mesoscale cyclones (Michel et al., 2018). To diagnose MCAOs, most
previous studies used a simplified version of the Brunt-Väisälä frequency for quantifying static stability, by considering only
the sign of the vertical temperature gradient between potential skin temperature of the ocean and potential air temperature aloft.
The temperature gradient is termed MCAO index, where positive potential temperature difference between the ocean surface
and the air aloft indicates vertical instability. Conventional MCAO indices (Papritz et al., 2015; Kolstad, 2017; Polkova et al.,
55 2019, 2021) have the form

$$m_\theta = \theta_{\mathrm{skin}} - \theta_{\mathrm{850hPa}}, \tag{1}$$

or variations thereof (Kolstad et al., 2009; Fletcher et al., 2016; Papritz and Sodemann, 2018; Landgren et al., 2019), where θ_{skin} is the potential skin temperature and θ_{850hPa} is the potential air temperature at 850 hPa. In what follows, we will summarize the different variants of previously-used MCAO indices using the term "conventional MCAO index". The vertical level at which

60   air aloft is considered for calculation of the conventional MCAO index (850 hPa in Eq. 1) will be referred to as the *characteristic pressure level*. The choice of the characteristic pressure level used for computing the MCAO index varies substantially amongst previous studies - from 500 hPa (Landgren et al., 2019), to 700 hPa (Kolstad et al., 2009), 800 hPa (Fletcher et al., 2016), 850 hPa (Papritz et al. (2015); Kolstad (2017); Polkova et al. (2019, 2021)) and 900 hPa (Papritz and Sodemann, 2018). Consequently, the magnitude of the MCAO index values, as well as the geographical extent of areas with positive MCAO

65   index values, differs between studies, and a classification into weak, moderate and strong MCAO events requires adjustment accordingly. The lack of consistency in the MCAO diagnostic, and the subjective choice of the characteristic pressure level at which the potential air temperature aloft is considered, complicates comparison of results from different studies and poses questions about the robustness and the mechanistic interpretation of the index. For example, which characteristic pressure level is most appropriate in which geographical region and time of the year? Is there a link between areas with high index values

70   and the occurrence of PLs? Is the projected frequency of occurrence of MCAOs in climatological assessments sensitive to details in the definition of the diagnostics used to measure MCAOs (such as, the choice of the characteristic pressure level)? In this study, we develop and test alternative diagnostic indices for MCAOs and PLs, which do not rely on the subjective choice of a characteristic pressure level, but instead measure key aspects of the vertical structure of MCAOs and PLs. We quantify the link between these indices and the time and location of observed PLs and propose a simple method for determining the

75   characteristic pressure level that maximizes the link to observed PLs.

The following key questions are adressed: how can we interactively explore 3-D features of meteorological phenomena, such as MCAOs and PLs, in ERA5 data? Is the 3-D structure of MCAOs and PLs resolved in ERA5? Can interactive 3-D visual data exploration help improving widely-used conventional MCAO indices, by motivating adaptations, new perspectives and options

80   for improvements? In the first part of this study, we extend and apply *Met.3D* (Rautenhaus et al., 2015b,a), a tool for interactive 3-dimensional visual analysis of gridded meteorological data, for case-studies of MCAOs and PLs. Based on insights from our interactive visual data analysis, we develop new diagnostic indices for MCAOs and PLs. In the second part of this study, we test these new indices by comparison with empirical data of observed PLs during years 2002-2011 in the Barents and the Nordic Seas from the STARS data set (Noer et al., 2011; STARS - data, 2013). .

2 Data and Methods

85

We designed a workflow starting with interactive 3-dimensional visual exploration of selected cases of MCAOs and PLs, followed by the development and testing of new diagnostic indices for characterizing MCAOs and PLs (see Fig. 1 for a summary of our workflow). The study was conducted in three steps: (1) develop and apply new methods for IVA of ERA5 to explore single cases of MCAOs and PLs (Sect. 2.1 and Sect. 2.2); (2) use insights from IVA of MCAOs and PLs for

90 conceptualizing improved diagnostic indices for MCAOs (Sect. 2.3); (3) evaluate the performance of the new indices, in comparison with conventional indices, by assessing associations with observed PLs (Sect. 2.4).
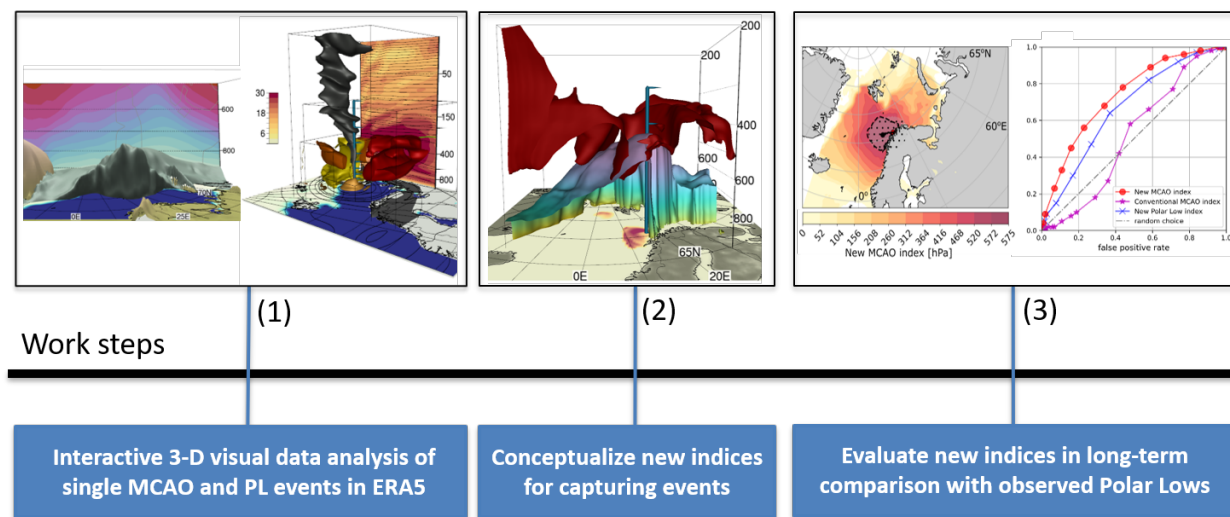
Figure 1. Summary of the workflow. We include 3-D interactive visual data analysis (IVA) into a workflow that bridges the gap between single case analyses and long-term assessments on seasonal to climatological time-scales. The following steps of analysis were conducted: (1) develop and apply new methods for IVA of ERA5 data to explore single cases of MCAOs and PLs (see Sect. 2.1 and Sect. 2.2); (2) use insights from IVA of MCAOs and PLs for conceptualizing improved diagnostic indices for MCAOs and PLs (see Sect. 2.3); (3) evaluate performance of diagnostic indices by comparison with observed PLs (see Sect. 2.4).

2.1 Develop new methods for IVA of ERA5

Our case-studies involving the development and application of methods for interactive visual analysis of MCAOs and PLs in ERA5 data confirm the usefulness of the visualization tool *Met.3D* (Rautenhaus et al., 2015b,a) for 3-D IVA of ERA5. The
95 current release (v1.7) of *Met.3D*, along with a set of sample scripts for download and post-processing of ERA5 data to the format required by *Met.3D* provide a toolset that can be used generically for 3-dimensional IVA of atmospheric phenomena in ERA5 (Met.3D - Homepage, 2021; Met.3D - Documentation, 2021; Met.3D - Documentation ERA5, 2021). *Met.3D* is a visualization tool with a graphical user interface that provides the user with various methods for interactive visual analysis of gridded meteorological simulation data (Rautenhaus et al., 2015b,a). Examples of available interactive visualization methods
100 include sliding horizontal and vertical cross-sections through data volumes, on-the-fly computation of 3-D isosurfaces, flow visualization techniques (streamlines and pathlines), as well as methods for ensemble-analyses. *Met.3D* is implemented in C++ and OpenGL with a focus on interactive useability, i.e. it has the capacity for user-defined, flexible and quick visual data exploration. As part of this study, we extend *Met.3D* by implementing two new features, of relevance to the IVA of ERA5 with particular focus on MCAOs and PLs: (i) support for processing polar stereographic data, as well as other common map

105   projections; (ii) on-the-fly computation of widely-used MCAO indices on user-defined vertical levels for visual assessment of the sensitivity to the choice of the characteristic pressure level in conventional MCAO indices.

2.2   Apply methods for IVA of ERA5 to MCAOs and PLs

Case-studies involving interactive 3-D visual data analysis using *Met.3D* were conducted for investigating MCAOs and PLs in ERA5. During the initial phase of our workflow, we selected a set of different exemplar cases for interactive 3-D visual analysis,
110   based on previous reports (Kolstad, 2011; Føre et al., 2012; Bracegirdle, 2012) about strong MCAO events and symmetric PLs (e.g. the case on Dec. 18, 2002 in Fig. 2 and 3). After the climatological analysis, we conducted additional interactive visual analyses in selected cases, for which the location of PL occurrence overlaps with the location of the highest MCAO index values (e.g. the case on Mar. 24, 2011 in Fig. 2 and 3). The following methods for explorative interactive visual analysis were used to study ERA5 during the times of selected MCAO and PL events: sliding horizontal and vertical cross-sections through
115   data volumes, exploration of the shape and location of 3-D isosurfaces of various data variables, direct volume rendering for inspecting cloud water and ice, computation of vector glyphs and streamlines of wind fields.

Our analyses are based on the recently released ECMWF's ERA5 reanalysis data with a spatial resolution of approximately 31 km horizontally, 137 vertical model levels, 37 pressure levels, and a hourly temporal resolution (Hersbach et al., 2020;
120   Copernicus Climate Change Service (C3S), 2017). We analyse data covering the time-interval 2002-2011, which is chosen to cover the times of observed PLs in the STARS data (Sect. 2.4). For the main part of our analyses, we use data from the ERA5 archive hosted at the German Climate Computing Center (copy of the original ERA5 archive; a total of 1.3 petabyte (DKRZ, 2020)). Additionally, we downloaded samples of data directly from the ECMWF for comparison and test of workflows (Copernicus Climate Change Service (C3S), 2017). The ERA5 data is remapped to a regular latitude-longitude grid using the
125   Climate Data Operators (CDO) (Schulzweida, 2020), as *Met.3D* requires a regularly spaced horizontal grid. The remapping of ERA5 was conducted on *Mistral*, the super-computer at the DKRZ. The remapped data was transferred to the regional computing center for visual data analysis of single cases. During the first phase of the visual case-analyses, we explored >10 ERA5 variables on a large geographical sub-domain (all longitudes; northern latitudes in the interval 25-90°; grid-dimension in lat-lon-height: 261×1441×137) for several cases of MCAOs and PLs to gain a first understanding, including large-scale
130   phenomena. During the second phase, we visually analysed single cases of MCAOs and PLs in more detail by inspecting ERA5 data variables (*t, pv, u, v, w, z, q, cc, ciwc, clwc*) on a smaller grid (440×440×137) with polar stereographic projection covering the Barents and the Nordic Seas. A total of around 3 TB of ERA5 data was probed by means of manual selection and visual data exploration. For interactive visual analysis in *Met.3D* all data that is rendered into a 3-D scene has to fit into the memory of a single GPU. New data is loaded on demand, when selecting new variables or manually stepping through time. For
135   the visual data analysis, we used a NVIDIDA Tesla T4 GPU in a vGPU setup with a global memory of 8 GB. Sample scripts for download and post-processing of ERA5 to the format required by *Met.3D* are available (Met.3D - Documentation, 2021; Met.3D - Documentation ERA5, 2021).

2.3 Use insights from IVA of MCAOs and PLs for conceptualizing improved diagnostic indices

Insights from the visual data exploration are interpreted and used as inspiration for developing improved diagnostic indices for
140   characterizing MCAOs and PLs in seasonal and climatological assessments based on widely available global meteorological datasets. The formulation of a new index is one of the objectives of this study and will be presented in Section 3.2. Newly introduced indices are tested in comparison with the conventional MCAO index with respect to their performance in distinguishing times and locations of PLs.

2.4 Evaluate performance of diagnostic indices by comparison with observed PLs

145   The conventional and the new MCAO index were tested by comparison with observed PLs, as reported in the STARS dataset (polar low tracks north) (STARS - data, 2013; Noer et al., 2011). The STARS dataset (in what follows referred to as STARS) contains 140 PLs observed during years 2002-2011 for the geographical region of the Barents and the Nordic Sea, including data about the times of PLs, the PL track and the approximate PL radius. For each PL, we rasterize the data about the observed track and radius to obtain a gridded representation of the area of past PLs in the form of a 2-D binary grid covering the geographical
150   cal domain of interest (latitudes: 57°N - 83°N, longitudes: 20°E - 66°E; chosen to cover the track of all PLs in STARS) where each grid-cell inside the area of observed PLs (track location plus radius) is set to one and all other grid-cells are set to zero. The binary data grid is compared with diagnostic index values calculated for each grid-cell in the same geographical domain. For 8 PLs in STARS, the approximate radius is not reported. As we require the empirically observed radius for defining the empirically observed area of past PLs, we sort out these 8 entries to ensure a consistent empirical dataset with 132 reported PLs.

155

In addition to the 132 PL events, we also compute the diagnostic indices for a set of "random pseudo-events", defined here as a time-interval of the same duration than the average duration of observed PLs, but during times when no PL was reported in STARS. The diagnostic indices are calculated during these randomly chosen control times, for investigating the robustness of the relationship between diagnostic indices and PLs not only during times of Polar Lows but also during "normal" weather
160   conditions (randomly chosen days). We define 132 control events, the same number as observed PLs, by randomly selecting times during October-March of years 2002-2011, when no PLs occurred.

The performance of diagnostic indices for distinguishing the time and location of occurrence of PLs is assessed by (i) visual analysis and comparison of index maps with maps of empirically observed tracks of PLs; (ii) automated counting of the num-
165   ber of matches between areas with high index values and locations of past PLs; (iii) Receiver Operating Characteristic (ROC) curve and accuracy score. For comparison of diagnostic indices with observed PLs, we compute for each grid-cell a temporal average, M_i, of the hourly index values (m_θ, m_p, m_{tr}; in what follows also denoted in summary as m_i, with $i \in \{\theta, p, tr\}$). The temporal average is computed over a time-interval that covers the reported time-interval of each PL in STARS. For the conventional and the new MCAO index, we compute the simple temporal average $M_i = \frac{1}{T} \sum_{t_0}^{t_{end}} m_i(t)$, where, $t_0 = t^*_{start} - 12h$
170   and $t_{end} = t^*_{stop} + 12h$ are the start and end times of the time-interval around each PL (t_{start}, t_{stop} are the reported start and

stop dates in STARS and we compute the index values for $\pm$ 12 hours to capture also environmental conditions around the genesis and end of PLs). For the new PL index we compute the temporal average over times with a lower-level instability as $M_{tr} = \frac{1}{T_{tr}} \sum_{t_0}^{t_{\text{end}}} \Theta(m_p(t)) \cdot m_{tr}(t)$, where t_0 and t_{end} as above, but T_{tr} is the number of hours with a lower-level instability and we only include in the temporal average the hourly index values, m_{tr}, for hours with lower-level instability ($m_p > 0$), and set the index to zero for all other hours (denoted here by the Heaviside-Theta function, $\Theta(m_p(t))$, which is 1 for all non-zero arguments ($m_p > 0$) and zero for all others). The different temporal average for the PL index, compared with the MCAO indices, is chosen because a lower-level instability (as indicated by a non-zero MCAO index) is assumed to be a necessary condition for the occurrence of PLs (following (Kolstad, 2011)) and we wanted to test if additional information about the upper level anomaly in the areas of MCAOs, as captured in m_{tr}, improves the performance of the index compared with the simpler new MCAO index.

The remapping of ERA5 data and the computation of the diagnostic indices for the 132 PL events and the 132 random pseudo-events were conducted on *Mistral* at the DKRZ. After selection of the required geographical sub-domain (Barents and Nordic Seas), time-intervals (covering all events) and remapping to regular grids, a total of approximately 1 TB ERA5 data were processed for computing the diagnostic indices.

3 Results and discussion

3.1 Interactive 3-dimensional visual analyses of MCAOs and PLs in ERA5

In this Section we provide selected examples from our interactive visual analyses in order to illustrate 3-D visualizations of MCAOs and PLs as represented in ERA5 (Fig. 2, Fig. 3; Movies 1-2). We demonstrate a workflow starting with explorative interactive visual analyses. The high resolution and consistency of ERA5 allows for both, detailed 3-D visual analyses of single cases of MCAOs and PLs (as reported in this Section), as well as long-term assessments of diagnostic indices used to capture these events (see subsequent Sections).

Our analyses show that 3-D features of the transport of cold air from sea-ice regions over the ocean during MCAOs are resolved in ERA5 and can be visually analysed, for example, by assessing the dynamics of the 3-D isosurface of potential temperature, illustrated here for two MCAO events in the Barents and the Nordic Sea (Fig. 2, Movie 1). During the MCAO event in December 2002 (Fig. 2a-c), the volume of cold-air grows in vertical extent before moving southward over the sea-ice into the Barents Sea. Complex spatio-temporal structures with great variation in shape and dynamics between different MCAO cases can be observed (e.g. Fig. 2d-f). Comparison with conceptual models and previous examples of standard 2-D depictions of MCAOs (see e.g. Gryschka (2018)) underline that advanced methods for 3-D visual analysis provide valuable additional perspectives and more realistic insights. While the visual inspection of cloud cover does partly resemble typical thick cloud bands at the boundary of the outbreak, as described e.g. in Gryschka (2018), the details of the characteristic 3-D structure of convective
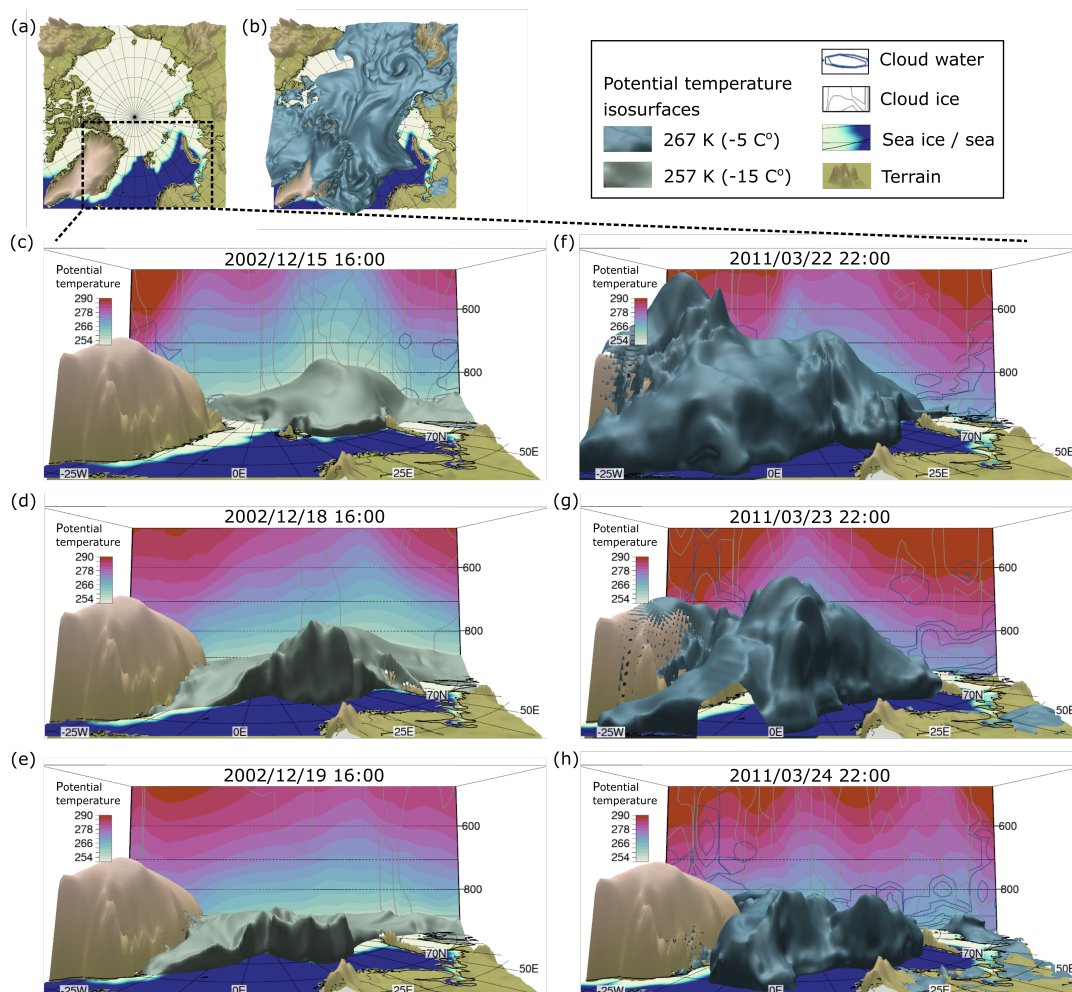
Figure 2. Three-dimensional interactive visual analysis of MCAOs in ERA5 data. Cold air is delineated by isosurfaces of potential temperature. The air below the isosurfaces has lower potential temperatures and the air above has higher potential temperatures. **(a - b)** show a top-view for locating the geographical domain of interest (Barents and Nordic Seas). Temporal snapshots illustrate the transport of cold air during two MCAOs. **(c - e)** Case 1: 2002/12/15-19; **(f - h)** Case 2: 2011/03/22-24. Before the start of the MCAO in case 1 **(c)**, the cold air is located above the sea-ice; it is then transported southward over the edge of the sea-ice onto open waters, forming a steep boundary at the edge of the convective region induced by the cold air moving over warmer oceans **(d - e)**. Case 2: **(f)** the cold air is partly transported over the top of Greenland and then **(g-h)** moves east into the Nordic Sea. Contour lines of cloud water and cloud ice are drawn at $10^{-5}, 10^{-6}, 10^{-8}$ [kg/kg]. Movie 1 demonstrates the interactive 3-D data exploration of MCAO case 1 using *Met.3D*. Fig. 3 illustrates winds during the PLs that formed within the MCAOs depicted here.

cloud bands, are not resolved in ERA5 for the cases we inspected (not shown).
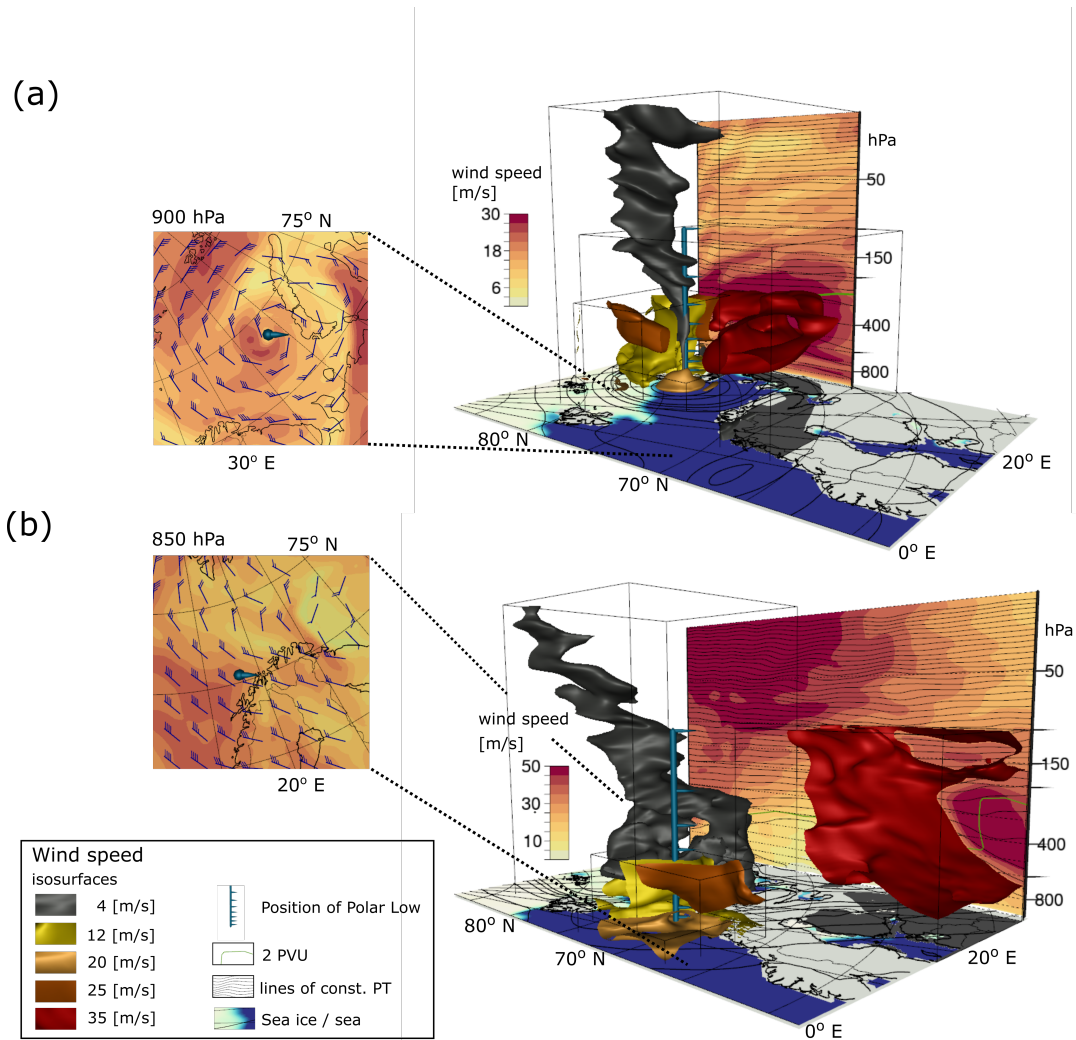
Figure 3. Three-dimensional interactive visual analysis of PLs in ERA5 data. Winds are visualized for the times of two PLs. **(a)** In case 1 - 2002/12/19 16:00, a symmetric slow wind "eye" is observed (gray isosurface) in the area where a PL is reported (Bracegirdle, 2012; Føre et al., 2012), with a pronounced vortex in the wind field around it (inlay with wind barbs). The tube-like, coherent volume of air with slow winds extends up into the stratosphere. As expected, fast winds are observed near the surface. Complex 3-D structures of the wind field in the lower troposphere are visualized by means of isosurfaces constrained to different bounding boxes for selective illustration of various wind speeds in different volumes of air in close proximity to the observed PL. The illustrated aspects of the 3-D wind field show similarities to previously described, typical 2-D wind-patterns during PLs (Michel et al., 2018). Movie 2 demonstrates the interactive 3-D data exploration of PL case 1 using *Met.3D*. **(b)** In case 2 - 2011/03/24 11:00, no symmetric slow wind eye is observed in the lower troposphere in the area of the reported PL (Noer et al., 2011). The jet-stream is stronger and located further south.

205   A PL that was described as an "Arctic hurricane" (Bracegirdle, 2012) formed east of the coast of Novaya Zemlya, during the 19-20th of December 2002, towards the end of the MCAO illustrated in Fig. 2. The capacity for quickly analysing various

data variables from different angles using different visualization methods is a key advantage of interactive 3-D visual data analysis, because it makes it easier to explore new perspectives and discover potentially interesting features. One such example emerging from our case-studies is a "slow wind perspective" on PLs (Fig. 3, Movie 2). During some of the PL events we

210 analysed, there is a coherent tube-like volume of air with slow wind speeds at the center of the PL which extends from the surface up into the stratosphere (e.g. winds < 4 m/s in Fig. 3a). This coherent 3-D feature of the wind field is consistent with the 2-D vertical profile of winds during reverse shear PLs (Michel et al., 2018), but here it is illustrated in 3-D and for a much larger vertical extent. Inspection of isosurfaces at different wind-speeds reveal complex wind flows during PLs, with strong near-surface winds (Fig. 3, Movie 2). Visual analysis of wind-barbs show vortex-like wind fields around the slow-wind eye. In-

215 teractive sliding of cross-sections through different vertical levels helps locating altitudes with strong winds as well as regions with strong wind shear (Movie 2). Resolved dynamics of cloud cover during the PL on the 19-20th of December 2002 hint at the observed symmetrical vortex of clouds during this PL (Bracegirdle, 2012), but details are not resolved in ERA5 (not shown).

3.2 Development of improved diagnostic indices for MCAOs and PLs

220 We implemented a new feature into *Met.3D* to compute widely-used conventional MCAO indices on-the-fly for analysing these indices during single MCAO events. Subsequently, we extended the formulation of the conventional 2-D MCAO index (Eq. 1) to 3-D. Inspecting its 3-D structure, unravels the sensitivity to changes in the characteristic pressure level (3.2.1). Aiming at improving diagnostic indices by avoiding the high sensitivity to the subjective choice of the characteristic pressure level, we focus on the vertical extent of MCAOs (3.2.2) and the vertical distance to the dynamical tropopause (3.2.3) when formulating

225 new diagnostic indices (3.2.4).

3.2.1 Sensitivity of conventional MCAO indices to the choice of the characteristic pressure level

Conventional MCAO indices have been calculated with a variety of different characteristic pressure levels - ranging from 500 hPa to 900 hPa - at which air aloft is considered for calculation of the MCAO index (Landgren et al., 2019; Kolstad et al., 2009; Fletcher et al., 2016; Papritz et al., 2015; Kolstad, 2017; Papritz and Sodemann, 2018; Polkova et al., 2019). For understanding

230 the 3-D structure of MCAOs and the sensitivity of conventional MCAO indices to the choice of the characteristic pressure level, we have implemented a functionality in *Met.3D* that allows for the interactive visual analysis of the effect of varying the characteristic pressure level. For this purpose, we introduce a simple 3-D extension of conventional MCAO indices. We compute the temperature difference between the surface and each vertical pressure level, p, instead of considering only one particular characteristic pressure level. That is, instead of the conventional MCAO index, $m_\theta = \theta_{\text{skin}} - \theta_{850\text{hPa}}$ (Papritz et al.,

235 2015; Kolstad, 2017; Polkova et al., 2019), we compute its 3-D variant

$$m_\theta^p = \theta_{\text{skin}} - \theta_p \tag{2}$$

and use methods for interactive visual analysis, such as sliding a horizontal cross-section through all vertical levels, p, of m_θ^p (Fig. 4, Movie 3). In a similar approach, we implement in *Met.3D* other variants of the conventional MCAO index (Kolstad

and Bracegirdle, 2008; Landgren et al., 2019; Fletcher et al., 2016).

240

Visual analyses of changes in m_θ^p at different locations when varying the characteristic pressure level show that the magnitude of MCAO index values as well as the geographical area with positive MCAO index values decreases with increasing altitude. At low altitudes, close to the ocean surface, potential air temperature is lower than potential skin temperature, leading to positive MCAO indices. At higher altitudes, potential air temperature increases, leading to negative MCAO indices (set to

245 zero in Fig. 4, Movie 3). Note that areas with extreme values of the conventional MCAO index, i.e. maximum temperature difference between the sea surface and a certain pressure level, do not necessarily coincide with areas where the conventional MCAO index is positive also at high altitudes (i.e. $m_\theta^p > 0$ at high vertical levels p; see Fig. 4, Movie 3). The magnitude of the MCAO index changes substantially with the choice of the characteristic pressure level, suggesting to reconsider the thresholds on distinguishing between weak, moderate and extreme MCAOs depending on the choice of the pressure level.

250

The sensitivity of conventional MCAO indices to the choice of the characteristic pressure level can be expected, considering standard vertical profiles of potential temperature along with a dynamic 3-D shape of the volume of cold air and its complex mixing with air masses above the ocean. With the aim of formulating a diagnostic index that is not sensitive to the choice of a characteristic pressure level, we consider in more detail the 3-D structure of potential air temperature.

255 ### 3.2.2 The upper boundary of MCAOs

The interactive visual analyses of the 3-D MCAO index, along with standard vertical profiles of potential air temperature, suggests that the vertical profile of potential air temperature in the column of air above each location inside of a MCAO may be sketched as follows: in the lower troposphere, there is an unstable layer of air, in which the potential air temperature decreases with altitude, followed by a layer with approximately constant potential air temperature, and then a stable layer of

260 air in which potential temperature increases with altitude. Fig. 4 shows the vertical profile of potential temperature at some exemplar locations. This implies that, in the column of air above each location (grid-cell) within the area of a MCAO, there should be at least one pressure level at which the 3-D MCAO index, m_θ^p, changes its sign. The critical pressure level, p^*, at which m_θ^p changes its sign is the altitude at which potential temperature aloft equals potential sea skin temperature,

$$\theta_{p^*} = \theta_{\text{skin}}. \tag{3}$$

265 The column of air below p^* is unstable and the air column above it is stable - with respect to the simple static stability criterion based on the difference in potential temperature aloft and at the surface, as used in in conventional MCAO indices (Landgren et al., 2019; Kolstad et al., 2009; Fletcher et al., 2016; Papritz et al., 2015; Kolstad, 2017; Papritz and Sodemann, 2018; Polkova et al., 2019). We therefore define the critical pressure level, p^*, as a simple measure of the upper boundary of MCAOs.

270 The upper boundary of the lower-level instability caused by MCAOs can be visualized by computing the zero-isosurface of m_θ^p. Visual analyses of the dynamics of the zero-isosurface reveal interesting spatio-temporal dynamics in the upper boundary of
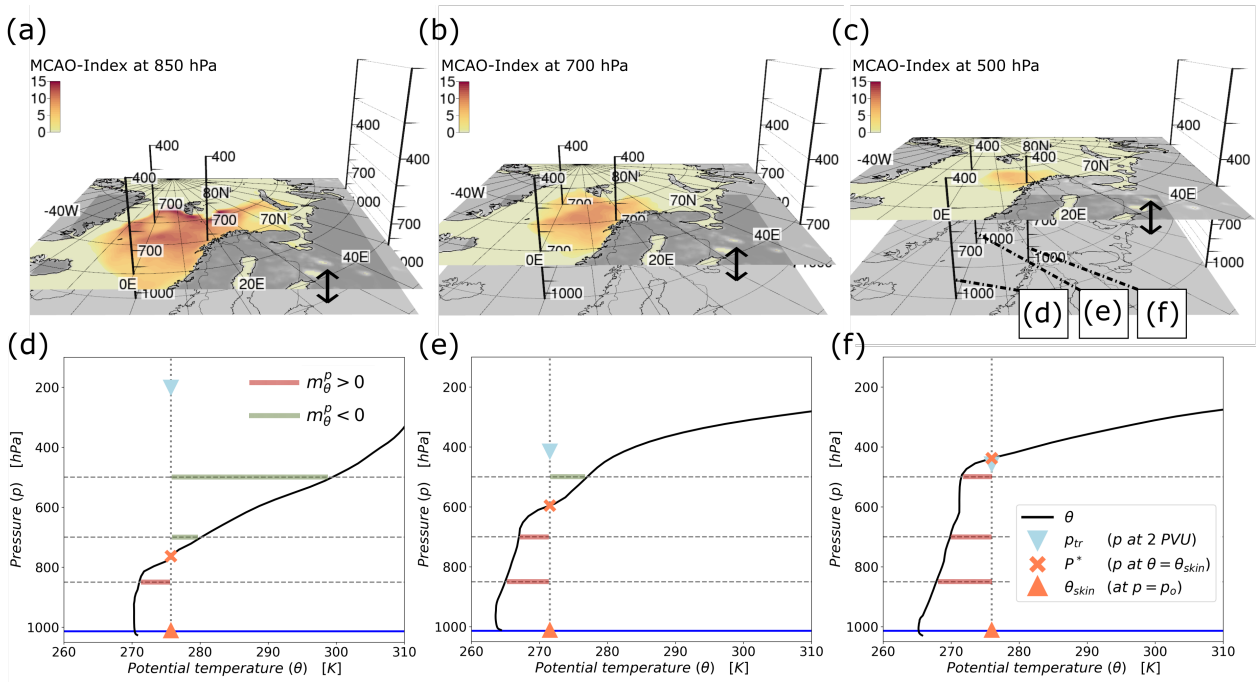
Figure 4. Extending the conventional MCAO index to 3-D. (a - c) Sensitivity of the conventional MCAO index to the choice of the characteristic pressure level. The MCAO index is calculated for the 24th of March 2011, 14:00 at different characteristic pressure levels (i.e. Eq. 2 with different values of θ_p): **(a)** 850 hPa; **(b)** 700 hPa; **(c)** 500 hPa. **(d -f)** Vertical profile of potential air temperature at selected locations within the MCAO (locations indicated by the poles in **(a-c)**). The 3-D variant of the conventional MCAO index is positive below and negative above the critical pressure level, p^* (illustrated as an orange cross), at which $\theta_{\text{skin}} = \theta_p$. The red and green lines illustrate the difference in potential temperature at the pressure levels shown in **(a - c)**. Movie 3 demonstrates the interactive visual analysis of the effect of varying the characteristic pressure level in the conventional MCAO index. Fig. 5 illustrates the 3-D structure of the MCAO shown here by visualizing the isosurface of p^*, as shown here **(d-f)** for exemplar positions, for the entire geographical domain.

MCAOs (Fig. 5, Movies 4-6). Investigation of several MCAO cases indicates a trend for the upper boundary of the lower-level instability to increase with distance from the sea-ice edge, which is in accordance with conceptual descriptions (Gryschka, 2018). However, there are substantial spatio-temporal variations during the course of single MCAOs and particularly between
275   different MCAOs. Interestingly, visual comparison of the upper boundary of MCAOs and the position of observed PLs during several of our use-cases shows that geographical areas with the highest vertical extent of MCAOs coincide with geographical areas of PLs. We therefore consider the upper boundary of the lower-level instability when deriving new diagnostic indices for characterizing MCAOs and PLs (Sect. 3.2.4).
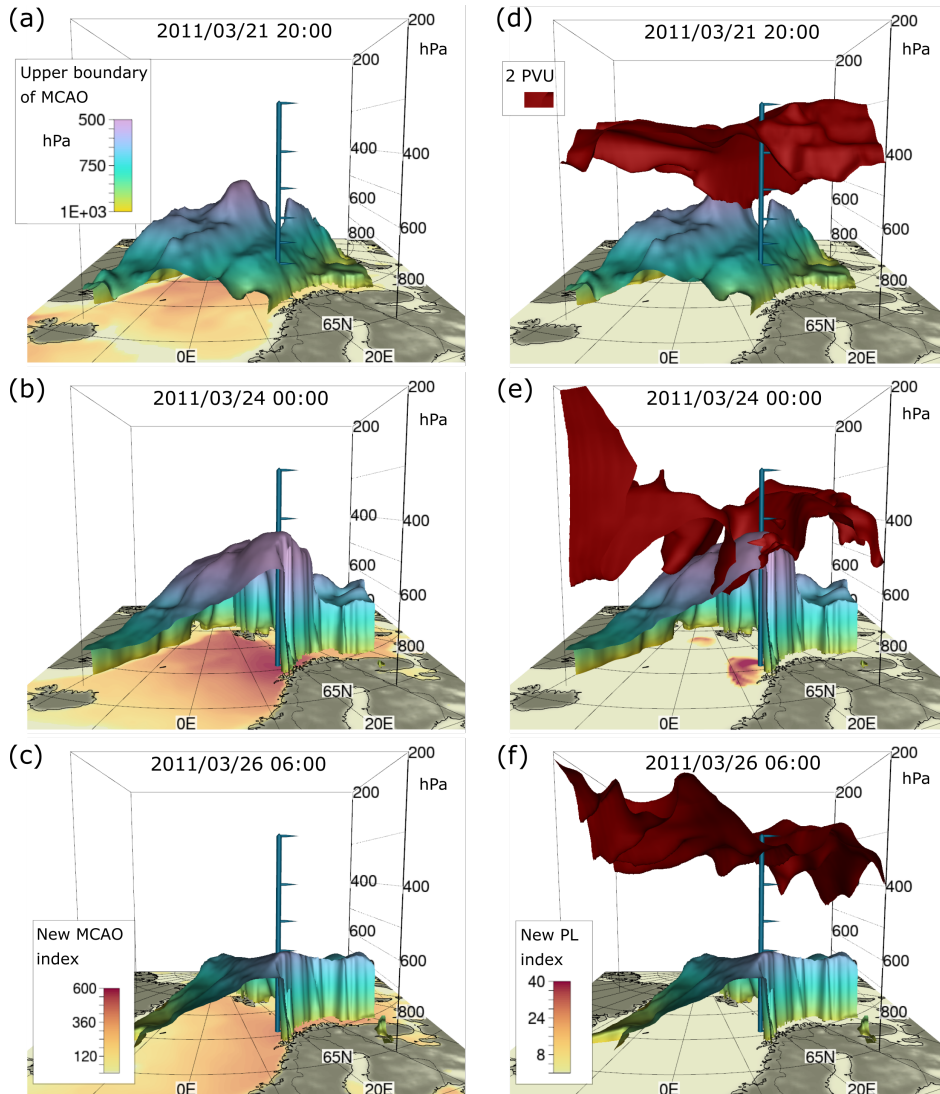
Figure 5. Upper boundary of a MCAO and its distance from the dynamical tropopause (a - c) Spatio-temporal variations in the upper boundary of a MCAO, defined here as the pressure level, p^*, at which $\theta = \theta_{skin}$. The new MCAO index, m_p (Eq. 4), which measures the pressure difference between the surface and p^*, is shown on the horizontal cross-section. **(d - f)** The dynamical tropopause extends downwards into the lower-level instability caused by the MCAO. Movies 4-5 show a time-lapse of 3D dynamics of the upper boundary and the dynamical tropopause for this case. Movie 6 shows a time-lapse of 3D dynamics of the upper boundary of the MCAO depicted in Fig. 2. We count the number of PLs in the STARS data for which the dynamical tropopause extends downward into the area of the MCAO and assess associations between areas with high vertical extend of MCAOs and observed PLs (see Fig. 6 and 7).

3.2.3 The vertical distance between lower-level instability and upper level anomaly during PLs

280 Both a lower-level instability and an upper-level forcing of the dynamical tropopause are required for PL genesis (Kolstad, 2011; Grønås and Kvamstø, 1995). Along these lines, Grønås and Kvamstø (1995) showed that, for 2 out of 4 PLs, the distance between the surface and the top of the atmospheric boundary layer was smaller than 2500 m. In related previous work Kolstad (2011) advocated that there was an association between PLs and the co-occurrence of two factors: a positive MCAO index and an upper-level potential-vorticity anomaly. Kolstad (2011) used these factors to define a binary PL index. Motivated by these

285 studies, we visually explore in *Met.3D* the spatio-temporal variations of the upper boundary of MCAOs (p^*, Eq. Sect. 3.2.2) in combination with spatio-temporal variations of the dynamical tropopause (defined here at 2 PVU, i.e. Potential Vorticity = $2 \cdot 10^{-6}$ [$\mathrm{Km^2 kg^{-1} s^{-1}}$]) (Fig. 5, Movie 5).

Interactive 3-D visual analysis of single cases indicates that the distance between the dynamical tropopause and the upper

290 boundary of MCAOs (Sect. 3.2.2) is smaller in geographic proximity to areas where PLs occur. During some of the PL cases, the dynamical tropopause extends downward into the lower-level instability region induced by MCAOs (Fig. 5e, crossing the zero-isosurface of m_θ^p with the dynamical tropopause; Movie 5). The distance between the dynamical tropopause and the lower-level instability region is therefore considered when formulating diagnostic indices for MCAOs and PLs (Sect. 3.2.4).

3.2.4 Characterizing MCAO and PLs with new diagnostic indices

295 Based on the insights from the 3-D IVA of selected cases, we introduce and test two new diagnostic indices: (i) the new MCAO index, and (ii) the new PL index. Put simply, the new MCAO index measures the vertical extent (in what follows also termed "height") of MCAOs, and the new PL index measures the vertical distance between the upper boundary of MCAOs and the dynamical tropopause. These metrics are designed to address shortcomings in conventional indices (subjective choice of pressure level and unclear relation of MCAOs to PLs) by taking into account 3-D features of the atmospheric circulation, while

300 remaining computationally cheap and hence feasible for use in climatological studies that rely on processing of large amounts of data (for details, see Sect. 3.3.4).

(i) New MCAO index: the index measures the vertical extent of the lower-level instability induced by MCAOs (expressed as a pressure difference). It is calculated for each horizontal grid-cell and time-step (hourly in ERA5) as the pressure difference

305 between the ocean surface and the upper boundary of the lower-level instability caused by a MCAO,

$$m_p = p_0 - p^*, \tag{4}$$

where p_0 is the constant surface pressure 1013.15 hPa. For the computation of the upper boundary of the MCAO, p^*, we determine the pressure level at which the potential air temperature equals the potential skin temperature. The new MCAO index m_p is set to 0 in grid-cells without lower-level instability. High index values of m_p correspond to high vertical extents of the

310 instability region caused by MCAOs.

Name	Definition	Unit	Required dimension of input data
Conventional MCAO index	$m_\theta = \theta_{\text{skin}} - \theta_{850\text{hPa}}$	[K]	2-Dimensional
3-D variant of the conventional MCAO index	$m_\theta^p = \theta_{\text{skin}} - \theta_p$	[K]	3-Dimensional
Region-specific variant of the conventional MCAO index	$m_\theta^{\text{crit}} = \theta_{\text{skin}} - \theta_{p_{\text{crit}}}$	[K]	2-Dimensional
New MCAO index	$m_p = p_0 - p^*$	[hPa]	3-Dimensional
New Polar Low index	$m_{tr} = p^* - p_{tr}$	[hPa]	3-Dimensional

Table 1. Diagnostic indices for measuring MCAOs. The term "conventional MCAO index" summarizes previously-used diagnostics that are based on the difference in potential temperature between the ocean surface and a fixed characteristic pressure level aloft, as e.g. 850 hPa (Papritz et al., 2015; Kolstad, 2017; Polkova et al., 2019, 2021), or others (Kolstad et al., 2009; Fletcher et al., 2016; Papritz and Sodemann, 2018; Landgren et al., 2019). The variants of the conventional MCAO index and the new indices are introduced and evaluated here for avoiding the subjective element in the choice of the characteristic pressure level and for capturing the vertical structure of MCAOs. Details of the indices are given in the text (see Eq. 1, 2, and 7 for the conventional MCAO index, its 3-D variant and a region-specific variant obtained by fitting to data about observed PLs; see 4 and 5, for the New MCAO, and New Polar Low index, respectively).

(ii) New polar low index: the index measures the "vertical distance" between the lower-level instability region induced by a MCAO and the dynamical tropopause. It is calculated for each horizontal grid-cell and time-step within the area of MCAOs ($m_p > 0$) as the pressure difference

315 $$m_{tr} = p^* - p_{tr}, \tag{5}$$

where p_{tr} (in hPa) is the pressure at the dynamical tropopause, which is defined at 2 PVU, and p^* is the pressure at the upper boundary of the MCAO. The new PL index decreases with decreasing distance between the dynamical tropopause and the lower-level instability and turns negative if the dynamical tropopause extends downwards into the lower-level instability induced by a MCAO.

320

The new indices suggested here and evaluated in subsequent Sections are summarized in Table 1, along with the conventional MCAO index and its variants.

3.3 Evaluating diagnostic indices by comparison with observed PLs

In previous Sections we summarized our case-studies of MCAOs and PLs, followed by the conceptualization of improved
325 diagnostic indices. Further on, we test the new metrics in comparison with the conventional MCAO index, for all PL events during years 2002-2011 occurring in the Barents and Nordic Seas (STARS data, (Noer et al., 2011; STARS - data, 2013)). In subsequent Sections, we show the distribution of index values in different geographical domains during all PLs (3.3.1), the number of matches between areas with high index values and areas where PLs have been observed (3.3.2), and the performance of indices in distinguishing times and locations of observed PLs from times and locations without PLs (3.3.3).

3.3.1 Diagnostic indices within and outside of observed PLs

Analysing the distribution of index values in all grid-cells during all years 2002-2011, within and outside of the areas of all observed PLs, shows: (i) high values of the conventional MCAO index occur only slightly more often in areas where PLs were observed, compared with all other areas in the domain (Fig. 6e); (ii) the new indices differ substantially between the two geographical domains - within and outside of observed PLs (Fig. 6b,h); (iii) high values of the new MCAO index and low values of the new PL index occur more often in geographical areas of the observed PLs compared with the rest of the domain (Fig. 6b,h).

The mean vertical extent of MCAOs within the area of all observed PLs during years 2002-2011, as captured by m_p (Eq. 4), is 289 hPa. Substantially higher vertical extents were observed (Fig. 6e), with a maximum at 607 hPa. In comparison, a mean vertical extent of 161 hPa is observed in areas outside of PLs. The mean vertical extent of MCAOs (289 hPa) corresponds to an upper boundary of the MCAO at $1013.15 - 289 \approx 724$ hPa and the maximum vertical extent corresponds to an upper boundary of the MCAO at approximately 406 hPa.

The mean distance between the upper boundary of the lower-level instability and the dynamical tropopause, as captured by m_{tr}, during all PL events is approximately 345 hPa, but substantially smaller distances are also observed (Fig. 6). Interestingly, in 41 % percent of all PLs, there is a short time of at least one hour during which the dynamical tropopause extends downward into the lower-level instability within the area of observed PLs ($p_{tr}(t) > p^*(t)$). In comparison, a larger mean distance of approximately 510 hPa was observed in the areas outside of observed PLs.

Investigating diagnostic indices during "pseudo-events", randomly selected times and locations when no PL occurred (see Sect. 2.4), shows that low values for the new MCAO index ("shallow" MCAOs) and larger values of the new PL index (low or absent forcing from the dynamical tropopause) occur more often during normal weather conditions than during PLs (gray bars in Fig. 6e-f and h-i). This suggests that the new indices capture features that are useful for distinguishing meteorological conditions during PLs from meteorological conditions during a randomly selected set of days in the Nordic winter.

3.3.2 Association between diagnostic indices and locations of observed PLs

The locations with high values of the new indices, m_p and m_{tr}, resemble the location of observed PLs for selected cases. For example, the area with high values of the new MCAO index during the MCAO case that we previously illustrated (Fig. 2, 4, and 5) matches the area of the observed PL remarkably well (Fig. 6), considering that it is a very simple index computed without using knowledge about the location of the PL or any fitting procedures.

We assessed for how many of all the PLs during years 2002-2011 in the Barents and Nordic Seas (as reported in the STARS data) there is an overlap between geographical areas with high values of the new MCAO index and geographical areas of
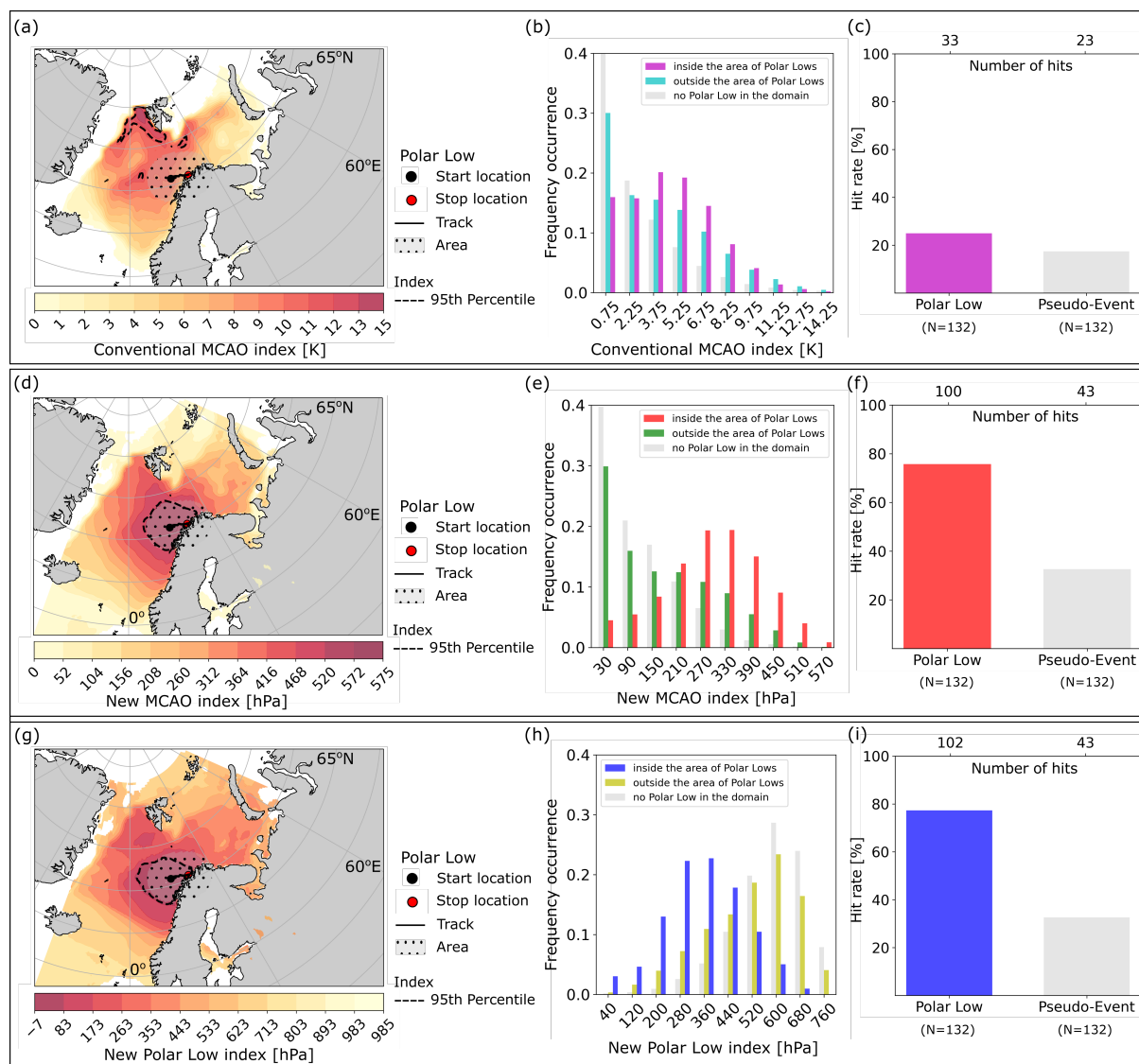
Figure 6. Association of diagnostic indices with locations of observed PLs. (a - c) Conventional MCAO index (Eq. 1); **(d - f)** new MCAO index (Eq. 4); **(g - i)** new PL index (Eq. 5). Maps **(a, d, g)**: Diagnostic indices for one selected example, the time of the PL on the 24th of March, 2011. PL track data (Noer et al., 2011; STARS - data, 2013). Histograms **(b, e, h)**: distribution of index values in all grid-cells for all PLs during years 2002-2011 separated into areas within and outside of the area of observed PLs. Gray bars show index values in all grid-cells of the domain during a set of randomly selected times with no PL (pseudo-events defined as a proxy for "normal" weather conditions without PLs; for details, see 2.4). Bar-charts **(c, f, i)**: number of overlaps between areas with high index values ($\geq$95-th percentile) and the area of observed PLs and random pseudo-events, respectively.

observed PLs (Fig. 6). The association is also analysed for the new PL index and the conventional MCAO index. We compute one diagnostic, M_i, for each PL event (time-average over all hours of the event; see Sect. 2.4), and use the 95-th percentile as

365 a critical threshold for delineating areas with "high" index values. We count the number of events with overlap of at least one grid-cell between areas with high index values and the area of observed PLs. Results for the new MCAO and PL indices show that, for approximataly 100 out of the total 132 observed PLs during years 2002-2011 (i.e., in approximately 76% of all cases), the area with high index values overlaps with the area of observed PLs (Fig. 6). This suggests a strong association between diagnostic indices and locations of PLs. In contrast, for the conventional MCAO index, areas with high index values only overlap

370 with areas of observed PLs in around 33 out of 132 PLs. Clearly, the association between high index values and locations of observed PLs is stronger for the new index values compared with the conventional MCAO index. PLs occurred more often in areas with high vertical extent of the lower-level instability rather than areas with strong instability at low altitudes.

The number of matches between areas with high index values and areas of observed PLs is sensitive to the choice of the

375 threshold for delineating "high" index values. We focus on testing the association between areas with particularly high index values ($\geq$95-th percentile), because these are confined to a fairly small area compared with the total geographical domain of the Nordic Seas which is a useful characteristic for an index that aims at narrowing down the likely location of PLs. Recall that MCAOs are relatively large-scale phenomena as compared to PLs. Thus as is, the conventional MCAO index is not a useful PL proxy in predictability studies as it indicates too large areas.

380

To assess if the number of matches that we obtain is substantially different to the number of matches one would expect by random choice of high index values somewhere in the geographical region of interest, we conduct the following test: We define a set of PL "pseudo-events" at times when no PL occurred and count the number of overlaps between these randomly selected areas with areas of high index values. Pseudo-event are defined by selecting at random an area that matches the average scale of

385 observed PLs (average track length and average radius; for details, see Sect. 2.4 for details). The number of matches between high index values and observed PLs is substantially higher than the number of matches between high index values and randomly chosen pseudo-events (Fig. 6), which provides additional supportive evidence for the robustness of the new diagnostics.

Results in this Section suggest that the new diagnostic indices are useful and informative for distinguishing the location of

390 PLs, given knowledge about the time of occurrence of PLs. For these new indices to be used in predictability studies or marine services as PL proxies, it is necessary to demonstrate that they are able not only to identify locations with higher risk for PLs, conditional on knowledge about the time of occurrence, but that they are able to distinguish times and locations of PLs without any prior knowledge from observations (as used in this and the last Section by analysing index values in detail for the times of observed PLs). This is tested in the next Section.

3.3.3 Performance of diagnostic indices in distinguishing the time and location of PLs

For assessing the performance of the new indices, we express the task of distinguishing the time and location of PLs based on diagnostic indices as a binary classification problem and assess ROC scores and accuracy. In a first step, we use the empirical STARS data to define an observed binary score of PL occurrence in all grid-cells (for details, see Sect. 2.4). For comparison of the binary empirical data about PL occurrence with the new indices, we introduce a critical threshold value, M_i^{crit}, to obtain a binary index, $\hat{M}_i$, from the continuous index values, M_i (Sect. 2.4), as follows

$$\hat{M}_i = \begin{cases} 1 & \text{if: } M_i > M_i^{\mathrm{crit}} \\ 0 & \text{if: } M_i \leq M_i^{\mathrm{crit}}. \end{cases} \tag{6}$$

The binary index values, $\hat{M}_i$, are computed for all grid-cells during all events, i.e. for observed PLs and for randomly chosen pseudo-events when no PL was observed. The binary indices are then analysed on the ability for distinguishing the time and location of the observed PLs. In the following, we first inspect the performance in distinguishing the time of occurrence of PLs and second the performance in distinguishing both the time and location of PLs based on the set of different critical thresholds.

For distinguishing the time of occurrence of PLs, we use the following classification: (i) if the binary index values are positive ($\hat{M}_i > 0$) anywhere in the geographical domain of interest during a particular time, we define this as a "prediction" that a PL occurs at that time anywhere in the domain (true positives: a PL occurs during that time; false positives: a PL does not occur during that time); (ii) if the binary index, $\hat{M}_i$, is zero everywhere in the domain, we define this as a "prediction" that no PL occurs (true negatives: no PL occurs during that time; false negative: a PL occurs during that time). Different threshold values (covering the interval of all observed index values; see Fig. 6) are tested by means of a ROC analysis, computing sensitivity and specificity for each threshold (see Fig. 7). The ratio of times that the new index correctly identifies PL events defines the true positive rate and the ratio of times that the new index incorrectly identifies the PL events as the false positive rate. The two rates are then plotted against each other. For being counted as a good proxy for PLs, in our experimental setup with 50% observed PL events and 50% non-events, it is necessary that the new index has an AUC score (area under the ROC curve) that is higher than 0.5. Our analysis shows that, all three diagnostic indices perform substantially better than random chance, suggesting that they could be useful for indicating the time of occurrence of PLs (AUC values of 0.78, 0.80 and 0.83, for the conventional MCAO index, the new PL index and the new MCAO index, respectively).

Additionally to the ROC analysis, we assess accuracy scores for the best threshold values determined in the ROC analysis. From the set of threshold values, $\hat{M}_i$, which are used in the ROC analysis for distinguishing the time of PLs, we select the one that maximizes Youdens Index (Youden, 1950), determined by the sum of sensitivity and specificity, as the best threshold. The best threshold for the conventional MCAO index to distinguish times of occurrence of PLs is 8 K (temperature difference). For the new MCAO index, it is 390 hPa, and for the PL index it is 250 hPa (as shown in Fig. 7). Using these thresholds to dichotomize the continuous index values, we compute the accuracy score for distinguishing the time of occurrence of PLs in the
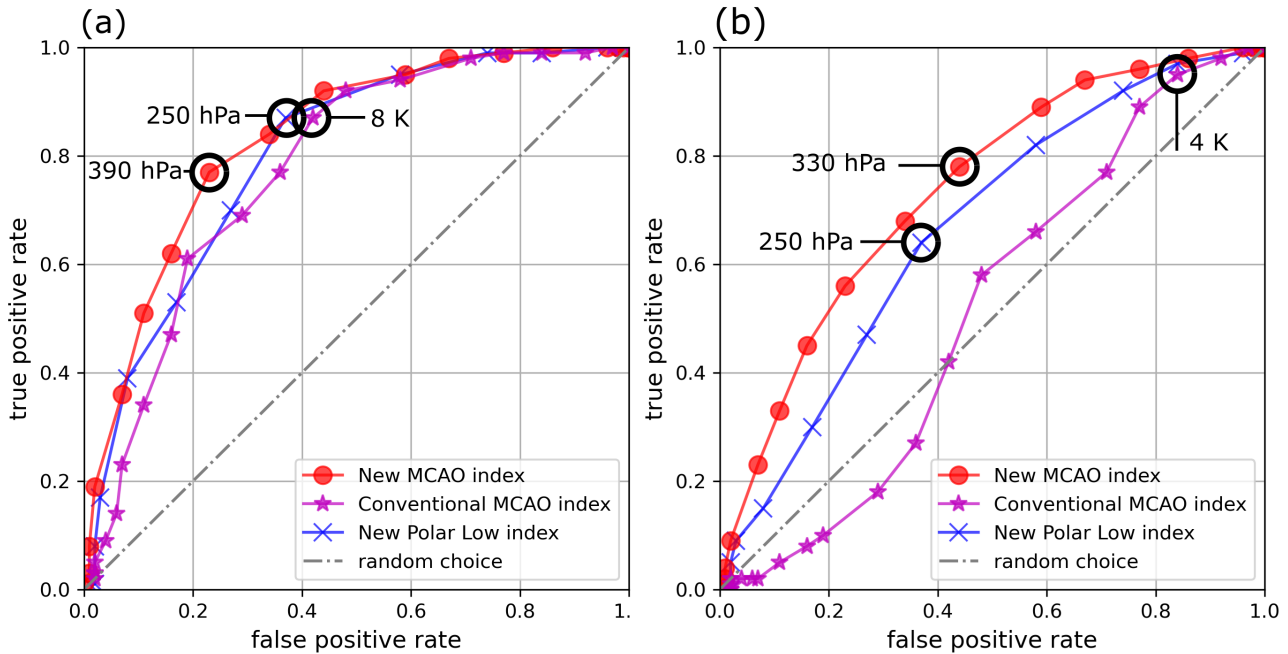
Figure 7. ROC curves for distinguishing times and locations of PLs based on conventional and new diagnostic indices. Panels: (a) time of PL events and (b) time and location of PL events. Index scores are compared with the times and locations of observed Polar Lows, as reported in the STARS data (Noer et al., 2011; STARS - data, 2013), by testing a set of critical thresholds (Eq. 6), for distinguishing areas and times at risk for Polar Lows. Diagnostic indices: the conventional MCAO index (Eq. 1), the new MCAO index (Eq. 4), and the new Polar Low index (Eq. 5). The critical thresholds highlighted in black are the best classifiers, defined as the thresholds $\hat{M}_i$ (Eq. 6) which maximize Youdens index (Youden, 1950). These are used for calculating the accuracy of indices in distinguishing times and areas of PLs (see text).

STARS data. In our experimental setup with the same number of PL events as non-PL "pseudo-events", an uninformed random classification would be expected to yield an accuracy score of 0.5. Using the conventional MCAO index with the threshold of 8 K, allows distinguishing the time of occurrence of PLs with an accuracy of 0.73. Using the new MCAO index with the
430   threshold of 390 hPa achieves an accuracy of 0.77. For the new PL index with a threshold of 250 hPa, we obtain an accuracy of 0.75.

For distinguishing the time and location of PLs, we use the following classification: (i) true positive, if there is an area with non-zero index values, $\hat{M}_i > 0$ (i.e. $M_i > M_i^{\mathrm{crit}}$), during a particular time and a PL is observed during that time in that area
435   (overlap of at least 1 grid-cell with the empirical data in STARS); (ii) false positive, if there is an area with non-zero index, $\hat{M}_i > 0$, during a particular time, but no PL is observed in that area at that time; (iii) true negative, if index values are zero, $\hat{M}_i = 0$, everywhere in the geographical domain during a particular time and no PL is observed anywhere in the domain during that time; (iv) false negative, if index values are zero everywhere in the geographical domain during a particular time, but

there is a PL observed somewhere in the domain during that time. Results of the ROC analyses show that the conventional
MCAO index performs poorly (close to random chance) in distinguishing the time and location of PLs (AUC value of 0.52).
This underlines that the magnitude of the conventional MCAO index is not useful for identifying times and locations at risk
for PLs. In contrast, the newly introduced indices perform substantially better in distinguishing the time and location of PLs
compared with the conventional MCAO index (AUC values of 0.67, and 0.74, for the new PL index and the new MCAO index,
respectively). Interestingly, the new MCAO index performs better than the new PL index, despite being simpler and requiring
less meteorological input data (the PL index requires the potential vorticity field as an additional 3-D data field).

The best threshold value for the new MCAO index that maximizes the sum of sensitivity and specificity in distinguishing the
times and locations of PLs in the ROC analysis is $M^{\mathrm{crit}} = 330$ hPa (thresholds for the other indices in Fig. 7). With this thresh-
old, we obtain a sensitivity of 0.78, a specificity of 0.58, and an accuracy of 0.67. In light of the complexitiy of PL genesis and
the simplicity of the new diagnostic index, the aforementioned performance (e.g. sensitivity of 0.78) is noteworthy. The new
MCAO index outperforms the conventional MCAO index and is better than uninformed random choice.

In summary, results from testing the performance of the conventional MCAO index and the new MCAO and PL indices (Sect.
3.3.1, 3.3.2, and 3.3.3), suggest the new MCAO index, m_p (Eq. 4), is a useful alternative to conventional MCAO indices for
serving as a proxy for PLs. The new index incorporates more information about the 3-D structure of cold air intrusions from
the Arctic and is more skilful in identifying areas and timing favourable for PL development.

3.3.4 Method for determining a region-specific characteristic pressure level for the conventional MCAO index from data about observed PLs

The new MCAO index (Eq. 4) is designed as a simple metric that requires processing of only one 3-D input data field (temper-
ature) for allowing its use in computationally expensive, long-term assessments that require processing large amounts of data.
While it is relatively straightforward to compute, it requires more input data compared with the conventional MCAO index,
which only requires 2-D input data. The implementation in e.g. predictability studies that compare multiple data sets might
therefore be challenging, depending on the available computational resources. To address this challenge, we suggest a simple
method that results in a computationally cheaper, region-specific variant of the conventional MCAO index, which maintains the
same quantitative link to observed PLs as the new MCAO index. Instead of using a subjectively chosen characteristic pressure
level for calculating the conventional MCAO index (Kolstad et al., 2009; Papritz et al., 2015; Fletcher et al., 2016; Kolstad,
2017; Papritz and Sodemann, 2018; Landgren et al., 2019; Polkova et al., 2019, 2021), we introduce a region-specific MCAO
index,

$$m_\theta^{\mathrm{crit}} = \theta_{\mathrm{skin}} - \theta_{p_{\mathrm{crit}}}, \tag{7}$$

and determine the critical characteristic pressure level, p_{crit}, that maximizes the link to observed PLs as follows:

1. compute the new MCAO index (Eq. 4) for a sufficient number of observed PL events in a certain geographical domain of interest, as well as for a set of randomly selected days without PLs (in this study, all PLs reported for years 2002-2011 in the Barents and the Nordic Seas and the randomly selected pseudo-events);

2. test different pressure levels as threshold values in a ROC analyses for distinguishing times and locations of observed PLs and select a threshold value, M_p^{crit} (Eq. 6) that maximizes a performance metric of choice (in this study, the threshold that maximizes the sum of sensitivity and specificity; Sect. 3.3.3).

3. compute the critical characteristic pressure level as

$$p_{\mathrm{crit}} = p_0 - M_p^{\mathrm{crit}}. \tag{8}$$

The region-specific MCAO index, m_θ^{crit}, has the advantage that it can be calculated based only on 2-D meteorological data fields, at the ocean surface and at p_{crit}, while maintaining the same skill in distinguishing the times and locations of PLs as compared to the new MCAO index, m_p (which requires processing the 3-D potential temperature field). Table 1 summarizes key differences between the region-specifc MCAO index and the other diagnostics considered in this study.

It becomes evident that the skill of the region-specific MCAO index, m_θ^{crit}, with a threshold of 0, is equivalent to the skill of the new MCAO index, m_p, with a threshold of M_p^{crit} when considering that all grid-cells in which the new MCAO index is higher than the critical threshold, M_p^{crit}, have positive values of the region-specific MCAO index. This is the case because the critical pressure level, p_{crit}, is vertically located below the upper boundary of the MCAO in all grid-cells in which the new MCAO index, m_p, is higher than the critical threshold, M_p^{crit} (combining Eqs. 4 and 8 shows that that $m_p > M_p^{\mathrm{crit}}$ implies $p_{\mathrm{crit}} > p^*$). The potential air temperature at the critical pressure level below the upper boundary of the MCAO is lower than the potential temperature at the upper boundary (for increasing potential temperature with height in the stable layers at the top of MCAOs; see Fig. 4 and Sect. 3.2.2). Hence it is also lower than the potential temperature at the ocean surface, because we define the upper boundary of the MCAO, p^*, to be the vertical level at which potential air temperature equals potential skin temperature (see Sect. 3.2.2). The region-specific MCAO index, which is calculated as the difference of potential temperature at the critical characteristic pressure level and the surface, has positive values in all grid-cells in which the new MCAO index is higher than the threshold value, M_p^{crit}. In short: if $m_p > M_p^{\mathrm{crit}}$, then $p_{\mathrm{crit}} > p^*$, which implies that $\theta_{p_{\mathrm{crit}}} < \theta_{p^*} = \theta_{\mathrm{skin}}$, so that $m_\theta^{\mathrm{crit}} > 0$, which means the skill based on $m_p > M_p^{\mathrm{crit}}$ is equivalent to the skill based on $m_\theta^{\mathrm{crit}} > 0$. This was confirmed by numerical analysis.

In practical terms, it means that using the region-specific MCAO index introduced in this Section with a threshold of 0 is equivalent to using the new MCAO index with a threshold of M_p^{crit} for distinguishing the times and locations of observed PLs. Positive values of the region-specific MCAO index distinguish times and locations of PLs with the same performance as the new MCAO index. While the procedure of determining the region-specific MCAO index is computationally expensive and requires processing of the 3-D potential temperature field, this only has to be conducted once for a specific geographical region in a baseline study for determining the critical characteristic pressure level by "fitting" to empirical data about PLs in

a specific region as outlined above. The resulting region-specific MCAO index is computationally cheap and thus feasible for
505 use in climatological assessments and for quick operational risk assessments as part of marine services.

4   Conclusions

We provide a showcase for the potential of 3-D interactive visual data exploration as part of the scientific workflow for advancing our understanding on meteorological phenomena. Designing a holistic workflow, we started with interactive visual exploration of selected cases of MCAOs and PLs, followed by the conceptualization of improved diagnostic indices, and
510 a proof-of-concept evaluation of the skill of the suggested new indices. Illustrated examples demonstrate the usefulness of *Met.3D* for interactive visual analysis of ERA5 data (Sect. 3.1). We reveal complex 3-D shapes of MCAOs and PLs and provide insights into features as detailed as the slow-wind eye of a PL (Sect. 3.1). Explorative visual analyses and climatological assessments underline that the vertical extent of the lower-level static instability caused by MCAOs, as well as the distance between the lower-level instability and the dynamical tropopause, can serve as better indicators for observed PL tracks than the
515 2-D MCAO index previously used in Landgren et al. (2019); Kolstad et al. (2009); Fletcher et al. (2016); Papritz et al. (2015); Kolstad (2017); Polkova et al. (2019); Papritz and Sodemann (2018).

We investigate a quantitative link between MCAOs and PLs by assessing the performance of MCAO indices in distinguishing times and locations of observed PLs (Sect. 3.3). Previous studies demonstrate that MCAOs are a necessary condition for PL
520 development (Ese et al., 1988; Noer et al., 2011; Kolstad, 2011; Mallet et al., 2013). However, what it is exactly about MCAOs that is decisive for PL occurrence is debated. For instance, Terpstra et al. (2020) suggests that the duration of MCAOs has no relation to PL initiation. Our study suggests that the new MCAO index allows narrowing down the area at risk for PLs, overcoming a disadvantage of the conventional MCAO index, which tends to identify too large areas at risk. Our results appear at odds with studies suggesting that PLs mostly happen outside of MCAOs (e.g., Terpstra et al., 2016). However, other authors
525 (Rasmussen, 1983; Kolstad, 2011) have pointed out that PLs happen also within MCAOs, especially those with warm-core thermal instability typically develop deep inside the polar air mass. Contradicting views in the literature might be related to defining subjectively the characteristic pressure level at which the conventional MCAO index is computed, as this implies a subjective element in the definition of the area of MCAOs. We address the challenges associated with the choice of the characteristic presure level by formulating alternative diagnostic indices that capture key features of the 3-D MCAO structure.

530

Results suggest that the new MCAO index (Eq. 4) is a promising candidate for use in long-term assessments on seasonal and climatological time-scales as it requires less input data (3-D temperature field and 2-D fields of surface pressure and skin temperature) than the new PL index and shows a slightly better skill (Sect. 3.3). Alternatively, we also suggest a method to determine the characteristic pressure level for the conventional MCAO index from empirical data about PL occurrence (Sect.
535 3.3.4). The revised 2-D MCAO index has the same form as the conventional index but avoids the subjective choice of the characteristic pressure level and provides a region-specific link to observed PLs. It is a good alternative to the new MCAO index, as

it is computationally cheaper and thus a more promising candidate for use in seasonal and climatological assessments, which usually compare the phenomena in multiple data sets over very long time-scales. An interesting line of future work would compare the predictability of the conventional and the new indices in a seasonal prediction system.

540

Our long-term assessment of the performance of conventional 2-D and new 3-D MCAO indices as proxies for PLs in the Barents and Nordic Seas (STARS data covering the time-period 2002-2011) shows that the new MCAO index performs better in distinguishing time and location of PLs compared with the conventional index (Sect. 3.3). While we show a statistical association between areas with high index values and PLs in a limited geographical and time-domain, our results (e.g. AUC and

545 accuracy scores in Sect. 3.3) also clearly highlight that the complex genesis of PLs cannot be fully captured with the simple diagnostic indices analysed here (both conventional and new indices). This can be expected considering the interplay of various factors that lead to PL genesis. More complex classification schemes, such as self-organising maps, have been reported very recently (Stoll et al., 2021). We focus on a simple diagnostic metric here for enabling its use in climatological assessments and seasonal forecasting systems. The association of areas with high values of the new MCAO index with the location of observed

550 PLs is promising. However, we have not distinguished between reverse shear and forward shear PLs in this analysis. Whereas front shear PLs are the most common ones, the reverse shear PLs are more easily detectable due to strong static instability conditions in the lower troposphere (Michel et al., 2018). Here, we use the criterion of static instability that is measured by the conventional MCAO indices (Kolstad and Bracegirdle, 2008; Kolstad, 2017).

555 In our analysis, we consider a set of pseudo-events for analysing the behaviour of indices during randomly selected weather conditions. A broader climatological assessment, computing hourly indices for time-intervals of several decades is beyond the scope of this study. Considering that PLs are rare events, the association between areas and times with high index values with areas and times of observed PLs might be overestimated. Future studies could build on this analysis, for example, by analysing longer PL data sets, such as provided in Rojo et al. (2019), taking into account different geographical areas and considering

560 alternative performance metrics, such as the extremal dependance index (EDI) (Wulff and Domeisen, 2019). If the performance of diagnostic indices shown in this study for a limited time-interval (2002-2011) and geographical region proof to be robust in other times and regions, then the new indices might be a useful complement for marine services on PLs.

The methods for 3-D interactive visual analysis of ERA5 data introduced here (Sect. 2.1, Sect. 3.1) are publicly available

565 (Met.3D - Homepage, 2021; Met.3D - Documentation, 2021; Met.3D - Documentation ERA5, 2021) and can be used generically, for interactive visual analysis of meteorological phenomena resolved in ERA5 data. We see great potential for using the open-source software *Met.3D* during the explorative phase of scientific workflows, as performed in this study, as well as for more detailed meteorological case-analyses.

570 *Code availability.* The code of the open-source visualization framework *Met.3D* is available at: https://gitlab.com/wxmetvis/met.3d. The Python and bash scripts for pre- and post-processing, statistical analyses and visualizations are available upon request.

Video supplement. The following movies illustrate interactive visual data analysis using *Met.3D* and provide supplementary insights into the 3-D dynamics of MCAOs and PLs in ERA5:

575
- **Movie 1**: Interactive visual data analysis of a Marine Cold Air Outbreak in ERA5 data.
- **Movie 2**: Interactive visual data analysis of a Polar Low in ERA5 data.
- **Movie 3**: Interactive visual data analysis of the characteristic pressure level in the conventional MCAO index.
- **Movie 4**: Dynamics of the upper boundary of a MCAO (time of MCAO: March, 2011).
- **Movie 5**: Dynamics of the upper boundary of a MCAO and the dynamical tropopause (time of MCAO: March, 2011).
580
- **Movie 6**: Dynamics of the upper boundary of a MCAO (time of MCAO: December, 2002).

Author contributions. Conceptualization: IP, MR, MM, JB; Study design and investigation: MM, IP, MR; Method development (*Met.3D*, Python, bash): MM, KMR, MR; Data Curation and Formal analysis: MM; Validation: MM, LS, IP, MR; Supervision: IP, MR, JB, SO; Visualization: MM, MR; Writing - original draft and preparation: MM; Writing - review and editing: MM, IP, MR, LS, KMR, JB, SO; Funding Acquisition: SO, JB, MR.

585 *Competing interests.* The authors declare that they have no conflict of interest.

Acknowledgements. We are grateful for the funding by the Deutsche Forschungsgemeinschaft (DFG, German Research Foundation) under Germany's Excellence Strategy – EXC 2037 'CLICCS - Climate, Climatic Change, and Society' – Project Number: 390683824, contribution to the Center for Earth System Research and Sustainability (CEN) of Universität Hamburg. We acknowledge funding provided by the Blue-Action project from the European Union's Horizon 2020 research and innovation programme under grant agreement No 727852. I.P. also
590 acknowledges funding from the Deutsche Forschungsgemeinschaft, Project number 436413914. The contribution of KRM to *Met.3D* code development, documentation and review of writing is funded by the sub-project ZZB of the Transregional Collaborative Research Centre (SFB/TRR165) - "Waves to Weather". We would also like to thank the DKRZ for providing an excellent research infrastructure, including the ERA5 data archive. Many thanks also to the Basis-Infrastruktur Group at the Regional Computing Center, Universität Hamburg, for maintainting the virtual GPU setup that was used for conducting parts of the analyses described here.

References

Aarnes, O., Kazuyoshi, M., and Morten Mejlaender, L.: End-user Requirements Specification Report Blue-Action Case Study Nr. 3 (D5.11), Zenodo, https://doi.org/10.5281/zenodo.1164217, 2018.

Afargan-Gerstman, H., Polkova, I., Ruggieri, P., King, M. P., Papritz, L., Athanasiadis, P., Baehr, J., and Domeisen, D. I.: Stratospheric influence on marine cold air outbreaks in the Barents Sea, Weather and Climate Dynamics Discussion, https://doi.org/https://doi.org/10.5194, 2020.

Ayachit, U.: The ParaView Guide: A Parallel Visualization Application, Kitware, Inc., New York, 2015.

Bracegirdle, T.: Artctic hurricane?, https://polarlows.wordpress.com/2012/02/08/130/, [last accessed: 3rd March, 2021], 2012.

Claud, C., Duchiron, B., and Terray, P.: Associations between large-scale atmospheric circulation and polar low developments over the North Atlantic during winter, Journal of Geophysical Research: Atmospheres, 112, 2007.

Clyne, J., Mininni, P., Norton, A., and Rast, M.: Interactive desktop analysis of high resolution simulations: application to turbulent plume dynamics and current sheet formation, New Journal of Physics, 9, 301–301, https://doi.org/10.1088/1367-2630/9/8/301, 2007.

Copernicus Climate Change Service (C3S): ERA5: Fifth generation of ECMWF atmospheric reanalyses of the global climate. Copernicus Climate Change Service Climate Data Store (CDS), https://cds.climate.copernicus.eu/cdsapp#!/home, 2017.

DKRZ: Deutsches Klimarechenzentrum. User Portal. ERA Data from the ECMWF, https://www.dkrz.de/up/services/data-management/projects-and-cooperations/era, [last accessed: 1st December, 2020], 2020.

Ese, T., Kanestrøm, I., and Pedersen, K.: Climatology of polar lows over the Norwegian and Barents Seas, Tellus A, 40, 248–255, 1988.

Fletcher, J. K., Mason, S., and Jakob, C.: A Climatology of Clouds in Marine Cold Air Outbreaks in Both Hemispheres, Journal of Climate, 29, 6677–6692, https://doi.org/10.1175/JCLI-D-15-0783.1, 2016.

Føre, I., Kristjánsson, J. E., Kolstad, E. W., Bracegirdle, T. J., Saetra, , and Røsting, B.: A 'hurricane-like' polar low fuelled by sensible heat flux: high-resolution numerical simulations, Q. J. R. Meteorolog. Soc., 138, 1308–1324, https://doi.org/10.1002/qj.1876, 2012.

Gryschka, M.: Polare Kaltluftausbrüche (Polar cold air outbreaks), pro*met*, 102, 44–55, 2018.

Grønås, S. and Kvamstø, N. G.: Numerical simulations of the synoptic conditions and development of Arctic outbreak polar lows, Tellus A: Dynamic Meteorology and Oceanography, 47, 797–814, https://doi.org/10.3402/tellusa.v47i5.11576, 1995.

Hersbach, H., Bell, B., Berrisford, P., Hirahara, S., Horányi, A., Muñoz-Sabater, J., Nicolas, J., Peubey, C., Radu, R., Schepers, D., Simmons, A., Soci, C., Abdalla, S., Abellan, X., Balsamo, G., Bechtold, P., Biavati, G., Bidlot, J., Bonavita, M., Chiara, G., Dahlgren, P., Dee, D., Diamantakis, M., Dragani, R., Flemming, J., Forbes, R., Fuentes, M., Geer, A., Haimberger, L., Healy, S., Hogan, R. J., Hólm, E., Janisková, M., Keeley, S., Laloyaux, P., Lopez, P., Lupu, C., Radnoti, G., Rosnay, P., Rozum, I., Vamborg, F., Villaume, S., and Thépaut, J.: The ERA5 global reanalysis, Q. J. R. Meteorolog. Soc., 146, 1999–2049, https://doi.org/10.1002/qj.3803, 2020.

Kolstad, E. W.: A global climatology of favourable conditions for polar lows, Q. R. J. Meteorolog. Soc., 137, 1749–1761, https://doi.org/10.1002/qj.888, 2011.

Kolstad, E. W.: Higher ocean wind speeds during marine cold air outbreaks: Higher Ocean Wind Speeds during Marine Cold Air Outbreaks, Quarterly Journal of the Royal Meteorological Society, 143, 2084–2092, https://doi.org/10.1002/qj.3068, 2017.

Kolstad, E. W. and Bracegirdle, T. J.: Marine cold-air outbreaks in the future: an assessment of IPCC AR4 model results for the Northern Hemisphere, Clim Dyn, 30, 871–885, https://doi.org/10.1007/s00382-007-0331-0, 2008.

Kolstad, E. W., Bracegirdle, T. J., and Seierstad, I. A.: Marine cold-air outbreaks in the North Atlantic: temporal distribution and associations with large-scale atmospheric circulation, Climate Dynamics, 33, 187–197, https://doi.org/10.1007/s00382-008-0431-5, 2009.

Landgren, O. A., Seierstad, I. A., and Iversen, T.: Projected future changes in Marine Cold-Air Outbreaks associated with Polar Lows in the Northern North-Atlantic Ocean, Climate Dynamics, 53, 2573–2585, https://doi.org/10.1007/s00382-019-04642-2, 2019.

Mallet, P.-E., Claud, C., Cassou, C., Noer, G., and Kodera, K.: Polar lows over the Nordic and Labrador Seas: Synoptic circulation patterns and associations with North Atlantic-Europe wintertime weather regimes, Journal of Geophysical Research: Atmospheres, 118, 2455–2472, 2013.

Met.3D - Documentation: User Documentation, https://collaboration.cen.uni-hamburg.de/display/Met3D/Userdocumentation, [last accessed: 4th of March, 2021], 2021.

Met.3D - Documentation ERA5: User Documentation ERA5, https://collaboration.cen.uni-hamburg.de/display/Met3D/Interactive3-DvisualanalysisofERA5reanalysisdata, [last accessed: 22nd of March, 2021], 2021.

Met.3D - Homepage: Interactive 3D visualization of meteorological (ensemble) simulations, https://met3d.wavestoweather.de/met-3d.html, [last accessed: 4th of March, 2021], 2021.

Michel, C., Terpstra, A., and Spengler, T.: Polar Mesoscale Cyclone Climatology for the Nordic Seas Based on ERA-Interim, Journal of Climate, 31, 2511–2532, https://doi.org/10.1175/JCLI-D-16-0890.1, 2018.

Noer, G., Saetra, , Lien, T., and Gusdal, Y.: A climatological study of polar lows in the Nordic Seas, Q. J. R. Meteorolog. Soc., 137, 1762–1772, https://doi.org/10.1002/qj.846, 2011.

Nordeng, T. E.: A most beautiful polar low. A case study of a polar low development in the Bear Island region, Tellus, 44, 81–89, 1992.

Papritz, L. and Sodemann, H.: Characterizing the Local and Intense Water Cycle during a Cold Air Outbreak in the Nordic Seas, Monthly Weather Review, 146, 3567–3588, https://doi.org/10.1175/MWR-D-18-0172.1, 2018.

Papritz, L. and Spengler, T.: A Lagrangian Climatology of Wintertime Cold Air Outbreaks in the Irminger and Nordic Seas and Their Role in Shaping Air–Sea Heat Fluxes, Journal of Climate, 30, 2717–2737, https://doi.org/10.1175/JCLI-D-16-0605.1, 2017.

Papritz, L., Pfahl, S., Sodemann, H., and Wernli, H.: A Climatology of Cold Air Outbreaks and Their Impact on Air–Sea Heat Fluxes in the High-Latitude South Pacific, Journal of Climate, 28, 342–364, https://doi.org/10.1175/JCLI-D-14-00482.1, 2015.

Polkova, I., Afargan-Gerstman, H., Domeisen, D., Ruggieri, P., Athanasiadis, P., King, M., and Baehr, J.: Marine Cold Air Outbreaks: Prediction Skill and Preconditions, in: Proceedings of the 9th International Workshop on Climate Informatics, p. 6, http://dx.doi.org/10.5065/y82j-f154, 2019.

Polkova, I., Afargan-Gerstman, H., Domeisen, D., King, M., Ruggieri, P. Athanasiadis, P., Dobrynin, M., Aarnes, O., Kretschmer, M., and Baehr, J.: Predictors and prediction skill for marine cold air outbreaks over the Barents Sea, QJRMS, https://doi.org/https://doi.org/10.1002/qj.4038, 2021.

Rasmussen, E.: A Review of Meso-Scale Disturbances in Cold Air Masses, in: Mesoscale Meteorology — Theories, Observations and Models. NATO ASI Series (Series C: Mathematical and Physical Sciences), vol. 114, Springer, Dordrecht, https://doi.org/10.1007/978-94-017-2241-4_13, 1983.

Rautenhaus, M., Grams, C. M., Schäfler, A., and Westermann, R.: Three-dimensional visualization of ensemble weather forecasts – Part 2: Forecasting warm conveyor belt situations for aircraft-based field campaigns, Geoscientific Model Development, 8, 2355–2377, https://doi.org/10.5194/gmd-8-2355-2015, 2015a.

Rautenhaus, M., Kern, M., Schäfler, A., and Westermann, R.: Three-dimensional visualization of ensemble weather forecasts – Part 1: The visualization tool Met.3D (version 1.0), Geoscientific Model Development, 8, 2329–2353, https://doi.org/10.5194/gmd-8-2329-2015, 2015b.

Rautenhaus, M., Bottinger, M., Siemen, S., Hoffman, R., Kirby, R. M., Mirzargar, M., Rober, N., and Westermann, R.: Visualization in
670   Meteorology—A Survey of Techniques and Tools for Data Analysis Tasks, IEEE Transactions on Visualization and Computer Graphics,
       24, 3268–3296, https://doi.org/10.1109/TVCG.2017.2779501, 2018.

Rojo, M., Claud, C., Noer, G., and Carleton, A. M.: In Situ Measurements of Surface Winds, Waves, and Sea State in Polar Lows Over the
       North Atlantic, Journal of Geophysical Research: Atmospheres, 124, 700–718, https://doi.org/10.1029/2017JD028079, 2019.

Schulzweida, U.: CDO User Guide (Version 1.9.9). Climate Data Operators., https://doi.org/10.5281/zenodo.4246983, 2020.

675 STARS - data: https://projects.met.no/polarlow/stars-dat/, [last accessed: 4th of March, 2021], 2013.

Stoll, P. J., Spengler, T., Terpstra, A., and Graversen, R. G.: Polar lows – moist-baroclinic cyclones developing in four different vertical wind
       shear environments, Polar lows, p. 18, 2021.

Terpstra, A., Michel, C., and Spengler, T.: Forward and Reverse Shear Environments during Polar Low Genesis over the Northeast Atlantic,
       Monthly Weather Review, 144, 1341–1354, https://doi.org/10.1175/MWR-D-15-0314.1, 2016.

680 Terpstra, A., Renfrew, I., and Sergeev, D.: Characteristics of Cold Air Outbreaks and associated Polar Mesoscale Cyclones in the North-
       Atlantic region, EGU General Assembly 2020, https://doi.org/https://doi.org/10.5194/egusphere-egu2020-22220, 2020.

Wulff, C. O. and Domeisen, D. I. V.: Higher Subseasonal Predictability of Extreme Hot European Summer Temperatures as Compared to
       Average Summers, Geophysical Research Letters, 46, 11 520–11 529, https://doi.org/10.1029/2019GL084314, 2019.

Youden, W. J.: Index for rating diagnostic tests, Cancer, 3, 32–35, https://doi.org/10.1002/1097-0142, 1950.